ELSEVIER

Atmospheric Environment 38 (2004) 1839–1850

ATMOSPHERIC ENVIRONMENT

www.elsevier.com/locate/atmosenv

Evolution of nanoparticle size and mixing state near the point of emission

Mark Z. Jacobson[a,*], John H. Seinfeld[b]

[a] *Department of Civil and Environmental Engineering, Stanford University, Terman M-31, Stanford, CA 94305-4020, USA*
[b] *Departments of Chemical Engineering and Environmental Science and Engineering, California Institute of Technology, Pasadena, CA 91125, USA*

Received 2 October 2003; accepted 20 January 2004

Abstract

This study examines the evolution of the size distribution and mixing state of soot and background particles near a point and line source of emission. This evolution occurs invariably at a spatial scale smaller than that of the grid scale of urban through global atmospheric models, and the evolved distribution is that which is properly the source distribution "emitted" into such models. A recent set of field data showed that, within minutes of emission, the soot particle size distribution evolved substantially, and it was hypothesized that Brownian coagulation was the main cause of the evolution. Here, it is found that Brownian coagulation, alone, may be insufficient to account for the observed rapid evolution of the size distribution. Enhancement of Brownian coagulation due to van der Waals forces offset by viscous forces and fractal geometry may account for a greater share of the evolution. These coagulation processes are represented together with aerosol emissions, nucleation, condensation, dissolution, hydration, and chemistry among 10 aerosol classes in a high-resolution three-dimensional numerical simulation. Dilution is found to be more important than coagulation at reducing the total number concentration of particles near the source of emission, but the relative importance of dilution versus coagulation varies with concentration. It is also found that heterocoagulation of emitted soot with background particles produces new mixtures in increasing concentration with increasing distance from the emission source. However, self-coagulation of emitted soot reduces particle number concentration by an order of magnitude more than does heterocoagulation of emitted soot with background particles in the first few minutes after emission. Heterocoagulation increases in relative importance as emitted particles age.

Keywords: Nanoparticles; Coagulation; Dilution; Three-dimensional modeling; Fractals

1. Introduction

The purpose of this paper is to examine the evolution of vehicle-exhaust particle size and mixing state near the point of emission. Measurements suggest that gasoline and diesel vehicles emit "nanoparticles" (<50 nm diameter), and diesel vehicles also emit "accumulation-mode particles" (50–1000 nm diameter) (e.g., Weingartner et al., 1997a; Kittelson, 1998; Maricq et al., 1999; ACEA, 1999; Shi et al., 2001; Harris and Maricq, 2001; Abu-Allaban et al., 2002; Sakurai et al., 2003). Nanoparticles are generally volatile, containing primarily unburned lubricating oil and sulfate, and form during dilution and cooling of the exhaust (Kittelson, 1998; Sakurai et al., 2003). Accumulation-mode particles are mostly aggregates of tens to thousands of spherules that collide and coalesce during combustion. The spherules are comprised of graphite (black) carbon coated by lubricating oil, polycyclic aromatic hydrocarbons, and/or inorganic compounds (e.g., Steiner et al., 1992; Kittelson, 1998; Norbeck et al., 1998; Schauer et al., 1999; Wehner et al., 2001; Sakurai et al., 2003). In terms

*Corresponding author.
E-mail addresses: jacobson@stanford.edu (M.Z. Jacobson), seinfeld@caltech.edu (J.H. Seinfeld).

1352-2310/$ - see front matter © 2004 Elsevier Ltd. All rights reserved.
doi:10.1016/j.atmosenv.2004.01.014

of overall emission composition, one study found that diesel exhaust consisted of about 68% black carbon, 31% organic carbon, and 1% other material whereas gasoline exhaust consisted of about 32% black carbon, 61% organic carbon, and 7% other material (Norbeck et al., 1998). In the absence of aftertreatment, though, diesel vehicles emit 10–100 times greater particle mass and up to 10^5 times more particle number than do new gasoline vehicles (Harris and Maricq, 2001).

Once emitted, particles affect human, animal, plant, and microorganism health, visibility, building appearance, cloud formation, and regional and global climate. In particular, numerical models and laboratory experiments suggest that the radiative effects of particles are affected by their mixing state and size (e.g., Ackerman and Toon, 1981; Chylek et al., 1988; Jacobson, 1997; 2000; Fuller et al., 1999; Chung and Seinfeld, 2002; Schnaiter et al., 2003). Recent field data have shown that the size distribution of emitted particles evolves substantially within a few hundred meters of emission (e.g., Hitchins et al., 2000; Shi et al., 2001; Zhu et al., 2002a, b). Zhu et al. (2002a), for example, found that the number of small particles decreased to a greater extent than did the number of large particles with increasing distance from a freeway, suggesting coagulation played a dominant role in the evolution of the size distribution. Because the evolution of particle size and mixing state starts at the point of emission and proceeds rapidly, it is important to examine the evolution near the source at high spatial and temporal resolution. This is especially true for urban to global scale atmospheric modeling since this evolution invariably occurs at a spatial scale smaller than that of the intrinsic model grid scale, and the evolved distribution is that which is properly "emitted" into the model.

To date, modeling studies of vehicle particle emissions have examined the evolution of a single size distribution near the point of emission with zero-dimensional (0-D) models (Vignati et al., 1999; Kim et al., 2002; Pohjola et al., 2003), a 1-D model (Capaldo and Pandis, 2001), and a 3-D model (Gidhagen et al., 2003). However, no study has examined the near-source evolution of multiple aerosol size distributions with a 3-D model. Here, 0-D and 3-D aerosol simulations that treat multiple distributions and interactions among them are carried out to examine the evolution of particles emitted from vehicles.

The 3-D simulations include point and line-source cases. Although the simulations are patterned to some extent after the field experiment of Zhu et al. (2002a), it is not possible to replicate their data without additional measurements (e.g., high-resolution meteorological observations, including turbulence parameters; information about the spatial variation of background aerosol composition, information about time- and location-dependent emissions at the freeway and nearby, and gas-phase emissions of condensable organics from the vehicles). Nevertheless, results here are compared to some degree. Results are also analyzed in terms of the relative importance of self- versus heterocoagulation and of coagulation versus dilution on particle evolution.

2. Description of the simulations

The model used was GATOR-GCMOM a global-through-urban scale air pollution/weather forecast/climate model (e.g., Jacobson, 1997, 2001, 2002). It treats gas, size-, composition-, and distribution-resolved aerosol, radiative, dynamical, cloud, and surface processes. For the present 3-D simulations, we selected an area of high motor vehicle emission, characteristic of any source of this nature. The model was run over a single, high-resolution limited-area grid (100 W–E cells $\times$ 60 S–N cells $\times$ 22 layers at a resolution of 15 m $\times$ 15 m in the horizontal and 5 m in the vertical), situated in West Los Angeles near the intersection of Interstate 405 and Wilshire Boulevard. The 3-D simulations were run for only a few minutes on a summer afternoon, so clouds and nesting from larger scales were neglected. The dynamical calculation was hydrostatic (Lu and Turco, 1995). Given that the terrain over the grid was relatively uniform and the time step for dynamics was limited to about 0.04 s by the horizontal grid spacing (15 m) divided by the speed of sound (346 m s^{-1} at 298 K), the hydrostatic assumption should have little effect on results. Meteorology was initialized from NCEP reanalysis field at 0 GMT (1600 Local Standard Time) on 27 August 1987 and predicted thereafter. The turbulence closure scheme used was from Mellor and Yamada (1982). Other processes solved included radiative transfer, gas chemistry, dry deposition, sedimentation, and aerosol microphysics and chemistry.

For all simulations, 10 aerosol size distributions were treated (Table 1), each with either 50 bins (for 0-D) or 17 bins (for 3-D). The distributions included five externally mixed distributions for which the only source of new particle number was emission or homogeneous nucleation, four binary distributions for which the only source of new particle number was coagulation between two externally mixed distributions (one of which was always emitted soot), and one well-internally mixed distribution for which the only source of new particle number was coagulation between a binary distribution and any other distribution or between two distributions that did not include emitted soot. Only four distributions (sea spray, soil, sulfate, and background soot) were initialized (Fig. 1).

Each bin in each distribution could hold up to 12 components (Table 1). Emitted and homogeneously nucleated species in appropriate distributions are listed

Table 1
Components in and sources of new particles in each size distribution

Distribution name	Symbol	Potential components	Initialized?	Source of new particles
Sea spray	A	H_2O, H^+, Na^+, NH_4^+, H_2SO_4(aq), HSO_4^-, SO_4^{2-}, NO_3^-, Cl^-, SOM	Yes	Em
Soil	B	Soildust, H_2O, H^+, NH_4^+, H_2SO_4(aq), HSO_4^-, SO_4^{2-}, NO_3^-, Cl^-, SOM	Yes	Em
Sulfate	D	H_2O, H^+, NH_4^+, H_2SO_4(aq), HSO_4^-, SO_4^{2-}, NO_3^-, Cl^-, SOM	Yes	Nuc
Emitted soot (ES)	E	BC, POM, SOM, H_2O, H^+, NH_4^+, H_2SO_4(aq), HSO_4^-, SO_4^{2-}, NO_3^-, Cl^-	No	Em
Background soot (BS)	F	BC, POM, SOM, H_2O, H^+, NH_4^+, H_2SO_4(aq), HSO_4^-, SO_4^{2-}, NO_3^-, Cl^-	Yes	None
Spray-ES	AE	H_2O, H^+, Na^+, NH_4^+, H_2SO_4(aq), HSO_4^-, SO_4^{2-}, NO_3^-, Cl^-, BC, POM, SOM	No	Co
Soil-ES	BE	Soildust, H_2O, H^+, NH_4^+, H_2SO_4(aq), HSO_4^-, SO_4^{2-}, NO_3^-, Cl^-, BC, POM, SOM	No	Co
Sulfate-ES	DE	H_2O, H^+, NH_4^+, H_2SO_4(aq), HSO_4^-, SO_4^{2-}, NO_3^-, Cl^-, BC, POM, SOM	No	Co
BS-ES	FE	BC, POM, SOM, H_2O, H^+, NH_4^+, H_2SO_4(aq), HSO_4^-, SO_4^{2-}, NO_3^-, Cl^-	No	Co
Internal mixture	MX	H_2O, H^+, Na^+, NH_4^+, H_2SO_4(aq), HSO_4^-, SO_4^{2-}, NO_3^-, Cl^-, BC, POM, SOM	No	Co

Note: Em, emissions; Nuc, homogeneous nucleation; Co, coagulation; BC, black carbon; POM, primary organic matter; and SOM, secondary organic matter. Emitted species in sea spray include H_2O, Na^+, Cl^-, H_2SO_4(aq), HSO_4^-, and SO_4^{2-}. Emitted species in soil include generic soildust. Emitted species in emitted soot include BC, POM, H_2SO_4(aq), HSO_4^-, and SO_4^{2-}. Nucleated species in sulfate include H_2O, H_2SO_4(aq), HSO_4^-, and SO_4^{2-}. Condensing gases on all distributions include H_2SO_4 and SOM. Dissolving gases on all distributions include HNO_3, HCl, and NH_3. The liquid water content and H^+ of each bin is determined as a function of the relative humidity and ion composition from equilibrium calculations. All distributions are affected by self-coagulation loss to larger sizes and heterocoagulation loss to other distributions (except the MX distribution, which has no heterocoagulation loss).

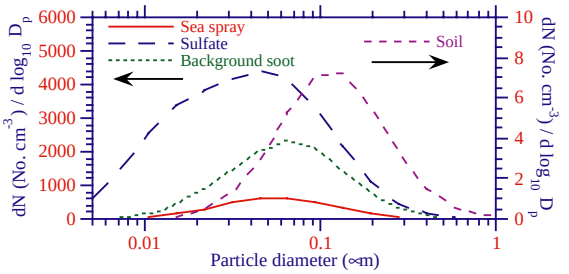

Fig. 1. Initial number distributions for the four initialized distributions in the 0-D and 3-D simulations.

in the footnote to Table 1. For the point-source calculation, soot was emitted into a single grid cell. The emission rate was 104.2 g-soot h^{-1} (2.5 kg-soot day^{-1}), which is the approximate emission rate of one unregulated heavy-emitting tractor. For the line-source calculation, the emission rate was 41 g-soot h^{-1} in each grid cell of the north–south freeway. This rate represents 17,000 "clean" passenger vehicles per hour passing through each 15-m grid cell and emitting 0.02 g $mile^{-1}$, plus 4000 "old" vehicles per hour emitting 0.3 g $mile^{-1}$ plus 3000 middle-aged trucks/buses per hour emitting an average of 1 g $mile^{-1}$. The 24,000 vehicles per hour is a typical peak vehicle flow rate on Interstate 405 in Los Angeles.

Fig. 4a of Zhu et al. (2002a) shows that, 30 m downwind of Interstate 405, the particle size distribution <100 nm contained three distinct modes. The first mode may have been the diesel nucleation mode, which peaks near 10–20 nm (e.g., Maricq et al., 1999; Abu-Allaban et al., 2002). One interpretation of the second mode (peaking at 27 nm diameter) is that it resulted from coagulation of the first mode. However, with a Brownian coagulation kernel, coagulation of a single mode generally moves the mode mean number diameter to a larger size rather than creating a second mode (e.g., Jacobson, 2002, Fig. 2a). A second mode can grow by coagulation most readily if a small second mode preexists. Thus, a second interpretation is that the second mode started as a gasoline nucleation mode, which peaks near 20–30 nm (e.g., Maricq et al., 1999; ACEA, 1999) or of a large nucleation mode of some diesel vehicles, and grew by coagulation. Because different motor vehicles are likely to emit at different sizes, it was assumed here that the second mode started

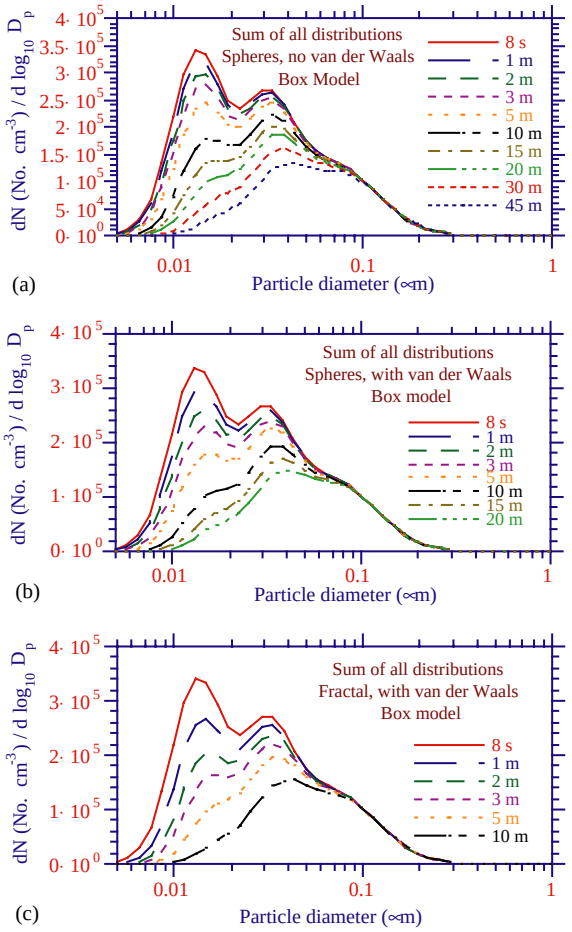

Fig. 2. Box-model calculation of the evolution of the sum of 10 aerosol distributions by coagulation when (a) particles are assumed spherical and no van der Waals or viscous forces are acting, (b) particles are assumed spherical and van der Waals and viscous forces are acting ($A/k_BT = 200$), and (c) particles are assumed fractal ($D_f = 1.7$) and van der Waals and viscous forces are acting ($A/k_BT = 200$). Other conditions were $T = 300$ K and $p = 1$ atm. The emitted soot distribution was initialized with no particles. Particles were emitted for 8 s after which, no more particles were emitted. No dilution was accounted for "m" = minutes and "s" = seconds.

as an emission mode. Thus, soot emissions here were distributed trimodally. The geometric mean number diameters and standard deviations were selected as 13 nm, 1.37; 30 nm, 1.40; and 68 nm, 1.68, respectively, based partly in Fig. 4a of Zhu et al. (2002a) and data from Harris and Maricq (2001). Emitted soot was assumed to consist of 68% BC, 31% OM, and 1% S(VI). Mass fractions of total BC emitted into the three modes were 0.002, 0.018, and 0.98, respectively, whereas those of OM and S(VI) were 0.01, 0.08, and 0.91, respectively. The difference accounts for the fact that the smallest diesel particles consist primarily of volatile material, whereas the largest are dominated by BC. The fractions of total particle number (accounting for all components together) emitted into each mode were approximately 0.44, 0.27, and 0.29, respectively.

In the model, self-coagulation moved particles and their components to larger sizes and decreased the number of particles in all distributions. Heterocoagulation moved particles and their components to different distributions. Table 2 summarizes the self- and heterocoagulation interactions treated. In addition, H_2SO_4 and secondary organic matter (SOM) were allowed to condense onto all distributions and HNO_3, HCl, and NH_3 dissolved in liquid water in all distributions. Condensable and soluble gases, including organics, were initialized in the model, and their concentrations evolved due to chemistry. Since the model did not resolve the tailpipe itself (horizontal resolution was 15 m), it was assumed that the emitted particle size distribution already accounted for condensation at the tailpipe. As such, emitted organic gases become condensable only after their oxidation to low-vapor-pressure species. The lifetime against reaction by OH of most condensable organic precursors (e.g., toluene, xylene) is generally longer than the 4-min simulation period. Aerosol liquid water and H^+ were calculated within each bin of each distribution with an equilibrium calculation. The numerical techniques used to solve homogeneous nucleation, coagulation, condensation, dissolution, and chemical equilibrium among multiple size distributions here are given in Jacobson (2002). Homogeneous nucleation and condensation are solved together. The nucleation, condensation, dissolution, and equilibrium schemes conserve gas-aerosol mass and particle number across all size distributions. The noniterative, semi-implicit coagulation scheme conserves volume and volume concentration across all size distributions and is positive-definite.

3. Van der Waals forces and fractal geometry

Zero-dimensional (box model) calculations were first run to test the effect of coagulation on the evolution of the emitted particle size distribution in the absence of dilution. The 10 size distributions in Table 1 were treated, four of which were initialized (Fig. 1). The emitted soot distribution was emitted for 8 s, and all aerosol physical processes described in Section 2 were permitted to affect all distributions during this period and thereafter. Initially, five coagulation processes were accounted for Brownian motion, Brownian diffusion enhancement, gravitational collection, turbulent inertial motion, and turbulent shear. Of the five, Brownian motion is by far the most important, causing 97.3% of

Table 2
Coagulation interactions

Size distribution name/symbol		Symbol of second distribution									
		A	B	D	E	F	AE	BE	DE	FE	MX
Sea spray	A	A	MX	MX	AE	MX	AE	MX	MX	MX	MX
Soil	B	MX	B	MX	BE	MX	MX	BE	MX	MX	MX
Sulfate	D	MX	MX	D	DE	MX	MX	MX	DE	MX	MX
Emitted soot (ES)	E	AE	BE	DE	E	FE	AE	BE	DE	FE	MX
Background soot (BS)	F	MX	MX	MX	FE	F	MX	MX	MX	FE	MX
Sea spray-ES	AE	AE	MX	MX	AE	MX	AE	MX	MX	MX	MX
Soil-ES	BE	MX	BE	MX	BE	MX	MX	BE	MX	MX	MX
Sulfate-ES	DE	MX	MX	DE	DE	MX	MX	MX	DE	MX	MX
BS-ES	FE	MX	MX	MX	FE	FE	MX	MX	MX	FE	MX
Internal mixture	MX	MX	MX	MX	MX	MX	MX	MX	MX	MX	MX

Note: The table gives the symbol of the size distribution into which two particles from either the same or different distributions coagulate to. For example, when a sea spray particle (A) coagulates with an emitted soot particle (E), the resulting particle is a sea spray-emitted soot (AE) particle. When three or more externally mixed (A…F) distributions or an externally mixed and binary (AE…FE) distribution or two binary distributions combine, they enter the mixed (MX distribution). Thus, the combination of background soot (F) with sea spray-emitted soot (AE) gives a mixed particle (MX).

particle number loss in one 12-h simulation (Jacobson, 2002).

Fig. 2a shows the evolution of the sum of the 10 size distributions over time. The figure shows that the first peak disappeared in favor of the second peak of 40 nm after 30–45 min. The 8-s distribution in Fig. 2a is somewhat similar to Fig. 4a of Zhu et al. (2002a). However, Fig. 4d of Zhu et al. shows that their first peak (from their Fig. 4a) disappeared in favor of the second peak of 40–50 nm in only 1–2 min (their Fig. 4d is 120 m downwind of their Fig. 4a, and wind speeds were 1–2.5 m s^{-1}). Zhu et al. hypothesized that, because the number of small particles decreased significantly while the number of large particles did not, Brownian coagulation played a major role in the evolution of the nanoparticle size distribution. Based on the calculation in Fig. 2a here, it appears that Brownian coagulation alone may not be fast enough to account for the evolution of the size distribution found in Zhu et al.

Two factors affecting coagulation not considered to date in 3-D studies nor in tandem include van der Waals forces/viscous forces and fractal geometry. Van der Waals forces are weak dipole–dipole attractions caused by brief, local charge fluctuations in nonpolar molecules having no net charge. Viscous forces arise due to the fact that two particles moving toward each other in a viscous medium have diffusion coefficients smaller than that of the sum of the two individual coefficients because velocity gradients generated by one particle affect those of the other. Whereas van der Waals forces enhance the rate of coagulation, particularly of nanoparticles, viscous forces retard the rate of van der Waals force enhancement in the continuum regime (e.g., Marlow, 1981; Schmidt-Ott and Burtscher, 1982; Alam, 1987; Seinfeld and Pandis, 1998). Fractals are particles of irregular, fragmented shape. The calculation in Fig. 2a assumes that all particles are spherical. However, soot aggregates, in particular, have been shown to be fractal in nature. Treatment of aggregates as fractal particles increases the rate of coagulation (e.g., Mountain et al., 1986; Mulholland et al., 1988; Rogak and Flagan, 1992; Harris and Maricq, 2001; Artelt et al., 2003). An additional factor affecting coagulation is Coulomb forces. Such forces, though, are important only if an aerosol is charged to a far greater extent than its equilibrium charge, and this is unlikely to occur for two submicron particles (Seinfeld and Pandis, 1998).

Here, the Fuchs interpolation formula for the Brownian coagulation kernel was modified to account for fractal geometry and van der Waals and viscous forces. The treatment of fractal geometry follows that of Rogak and Flagan (1992), except that here, the Fuchs interpolation formula was used for the transition regime whereas in Rogak and Flagan, a different interpolation formula that gives similar results was used. The modified Brownian collision kernel between particles of sizes i and j (cm^3 $particle^{-1}$ s^{-1}) used here is

$$\beta_{i,j}^{B} = \frac{4\pi(r_{c,i}+r_{c,j})(D_{m,i}+D_{m,j})V_{i,j}}{\dfrac{r_{c,i}+r_{c,j}}{r_{c,i}+r_{c,j}+(\delta_{m,i}^2+\delta_{m,j}^2)^{1/2}}+\dfrac{4(D_{m,i}+D_{m,j})}{\sqrt{\bar{v}_i^2+\bar{v}_j^2}(r_{c,i}+r_{c,j})}}, \quad (1)$$

where $V_{i,j}$ is a correction factor accounting for van der Waals and viscous forces, r_c is a collision radius (cm), D_m is a particle diffusion coefficient (cm^2 s^{-1}) evaluated at the mobility radius, δ_m is a mean distance (cm) used in the Fuchs interpolation formula, evaluated at the

mobility radius, and $\bar{v}$ is the mean thermal speed ($\mathrm{cm\,s^{-1}}$) of a particle, which is affected by particle mass but not radius.

For spherical particles, the collision and mobility radii equal the volume-equivalent radius, r_i (cm), which is the radius of the particle as if it were a sphere of uniform density. As such, Eq. (1) simplifies to the Brownian kernel for spheres unaffected by van der Waals/viscous forces when $V_{i,j} = 1$.

For fractals, Rogak and Flagan (1992) suggest that the collision radius should lie between the fractal radius (outer radius of the agglomerate) and the mobility radius. They also found (in their Figure 10) that their modeled coagulation kernel matched measurements the best when the fractal (outer) radius was used as the collision radius. Here, the collision radius is assumed to equal the fractal radius, defined as

$$r_{\mathrm{f},i} = r_1 N_i^{1/D_\mathrm{f}}, \tag{2}$$

where $N_i = v_i/v_1$ is the number of individual spherules in the soot aggregate, $v_i = 4\pi r_i^3/3$ is volume of the aggregate as if it were a sphere of uniform density, r_1 and v_1 are the radius and volume of an individual spherule that makes up the aggregate, and D_f is the fractal dimension. Individual spherules in diesel soot are about 20–30 nm in diameter (e.g., Weingartner et al., 1997b; Wentzel et al., 2003; Naumann, 2003). A value of 27 nm is assumed here ($r_1 = 1.35 \times 10^{-6}$ cm). For spheres, $D_\mathrm{f} = 3$. Fractal dimensions for soot particles range from 1.5 to 2.5 (e.g., Harris and Maricq, 2001). Here, a value of 1.7 was assumed. The mobility radius used from Rogak and Flagan (1992) is

$$r_{\mathrm{m},i} = \mathrm{MAX}\left\{\frac{r_{\mathrm{f},i}}{\ln(r_{\mathrm{f},i}/r_1)+1},\ r_{\mathrm{f},i}\left(\frac{D_\mathrm{f}-1}{2}\right)^{0.7},\ r_{\mathrm{A},i}\right\}, \tag{3}$$

where

$$r_{\mathrm{A},i} = \begin{cases} r_1\sqrt{\mathrm{MAX}\{N_i^{2/3},\ \mathrm{MIN}[1+0.67(N_i-1),\ D_\mathrm{f}N_i^{2/D_f}/3]\}}, & r_i \geqslant r_1, \\ r_i, & r_i < r_1 \end{cases} \tag{4}$$

is the area-equivalent radius.

In Eq. (1), the particle diffusion coefficient is

$$D_{\mathrm{m},i} = \frac{k_\mathrm{B}T}{6\pi r_{\mathrm{m},i}\eta}\{1 + Kn_{\mathrm{m},i}[A' + B'\exp(-C'/Kn_{\mathrm{m},i})]\}, \tag{5}$$

where k_B is Boltzmann's constant, T is absolute temperature, η is the dynamic viscosity of air, A', B', and C' are experimentally derived constants 0.864, 0.29, and 1.25, respectively (Kasten, 1968), and $Kn_{\mathrm{m},i} = \lambda_\mathrm{a}/r_{\mathrm{m},i}$ is the Knudsen number (where λ_a is the mean free path of an air molecule). Also in Eq. (1), $\bar{v}_i = \sqrt{8k_\mathrm{B}T/\pi\bar{M}_i}$, where $\bar{M}_i$ is the mass of a single particle, and

$$\delta_{\mathrm{m},i} = \frac{(2r_{\mathrm{m},i} + \lambda_{\mathrm{m},i})^3 - (4r_{\mathrm{m},i}^2 + \lambda_{\mathrm{m},i}^2)^{3/2}}{6r_{\mathrm{m},i}\lambda_{\mathrm{m},i}} - 2r_{\mathrm{m},i}, \tag{6}$$

where $\lambda_{\mathrm{m},i} = 8D_{\mathrm{m},i}/\pi\bar{v}_i$ is the effective mean free path of a particle of size i.

The van der Waals/viscous correction factor was determined with an interpolation formula between the free-molecular and continuum regimes (Alam, 1987), adjusted here for fractal geometry with

$$V_{i,j} = \frac{W_{\mathrm{c},i,j}[1 + 4(D_{\mathrm{m},i} + D_{\mathrm{m},j})/\sqrt{\bar{v}_i^2 + \bar{v}_j^2}(r_{\mathrm{c},i} + r_{\mathrm{c},j})]}{1 + (W_{\mathrm{c},i,j}/W_{k,i,j})(4(D_{\mathrm{m},i} + D_{\mathrm{m},j})/\sqrt{\bar{v}_i^2 + \bar{v}_j^2}(r_{\mathrm{c},i} + r_{\mathrm{c},j}))}. \tag{7}$$

The individual correction factors for the free-molecular and continuum regimes are

$$W_{\mathrm{k},i,j} = \frac{-1}{2(r_i + r_j)^2 k_\mathrm{B}T}\int_{r_i+r_j}^{\infty}\left(\frac{\mathrm{d}E_{i,j}(r)}{\mathrm{d}r} + r\frac{\mathrm{d}^2E_{i,j}(r)}{\mathrm{d}r^2}\right) \times \exp\left[\frac{-1}{k_\mathrm{B}T}\left(\frac{r}{2}\frac{\mathrm{d}E_{i,j}(r)}{\mathrm{d}r} + E_{i,j}(r)\right)\right] r^2\,\mathrm{d}r, \tag{8}$$

and

$$W_{\mathrm{c},i,j} = \frac{1}{(r_i + r_j)\int_{r_i+r_j}^{\infty}\frac{D^\infty}{D_{i,j}}(r)\exp[E_{i,j}(r)/k_\mathrm{B}T]\frac{\mathrm{d}r}{r^2}}, \tag{9}$$

respectively. In these equations,

$$E_{i,j}(r) = -\frac{A}{6}\left[\frac{2r_ir_j}{r^2 - (r_i + r_j)^2} + \frac{2r_ir_j}{r^2 - (r_i - r_j)^2} + \ln\frac{r^2 - (r_i + r_j)^2}{r^2 - (r_i - r_j)^2}\right] \tag{10}$$

is the van der Waals interaction potential, in which A is the Hamaker constant, which depends on van der Waals properties of each substance (e.g., Seinfeld and Pandis, 1998). In Eq. (9),

$$\frac{D^\infty}{D_{i,j}}(r) = 1 + \frac{2.6r_ir_j}{(r_i + r_j)^2}\sqrt{\frac{r_ir_j}{(r_i + r_j)(r - r_i - r_j)}} + \frac{r_ir_j}{(r_i + r_j)(r - r_i - r_j)} \tag{11}$$

is a diffusion ratio that corrects the diffusion coefficient in the continuum regime for viscous forces. In the equation, $D_{i,j}$ is a "relative" diffusion coefficient between particles i and j, and $D^\infty = D_i + D_j$ is the sum of the individual diffusion coefficients of the two particles. In Eqs. (8)–(11), all terms were evaluated at volume-equivalent spherical radii to ensure consistency with the original equations. The integrals in the equations were discretized in the model.

Fig. 3 shows the van der Waals/viscous force correction factor $V_{i,j}$ versus particle pair Knudsen number, $Kn_\mathrm{p} = \sqrt{\lambda_{m,i}^2 + \lambda_{m,j}^2}/(r_{m,i} + r_{m,j})$, assuming

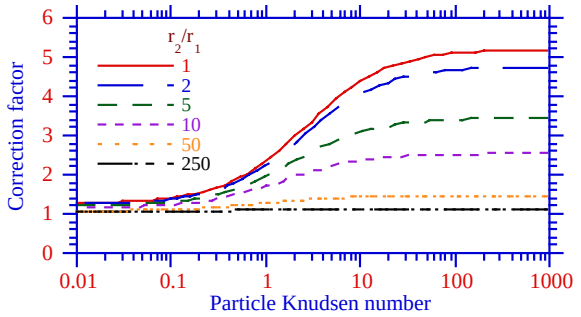

Fig. 3. Van der Waals/viscous force correction factor $V_{i,j}$ as a function of particle Knudsen number and different ratios of the radii of two interacting particles when $T = 300\,\mathrm{K}$, $p = 1\,\mathrm{atm}$, particle density $= 1\,\mathrm{g\,cm^{-3}}$, and $A/k_\mathrm{B}T = 200$.

spherical particles for the figure and $A/k_\mathrm{B}T = 200$, the value used in the 3-D simulations discussed here. A figure for $A/k_\mathrm{B}T = 20$, not shown, produces results exactly the same as those in Alam (1987, Fig. 5). Fig. 3 here shows that van der Waals forces enhance the coagulation rate of small particles (high Kn_p) by up to a factor of five when $A/k_\mathrm{B}T = 200$. The modeled enhancement factor for two 10-nm diameter particles ($Kn_\mathrm{p} = 4.5$) is about 3.75. Data from Okuyama et al. (1984) suggest the enhancement factor for silver particles can reach nine, suggesting that $A/k_\mathrm{B}T = 200$, used here, may be an underestimate. The measured enhancement factor of nine could be accomplished with Eq. (7) if $A/k_\mathrm{B}T = 1300$, but such a high value for diesel soot is uncertain.

Fig. 4 shows the effect of van der Waals/viscous forces and fractal geometry on the Brownian collision kernel. Van der Waals forces enhanced the kernel less for fractals than for spherical particles because, for the same volume-equivalent diameter, a fractal is more likely than a spherical particle to be in the transition or continuum regime than the free-molecular regime, and van der Waals forces are weakest in the continuum regime. Fig. 4 also shows that, when one particle was small (10 nm), fractal geometry increased the kernel with increasing size of the second particle. When one particle was larger (100 nm), fractal geometry enhancement was minimized when the second particle was also 100 nm.

Figs. 2b and c show the effect of van der Waals/viscous forces and fractal geometry on the size distribution of aerosols simulated in Fig. 2a. Fig. 2b shows that treatment of van der Waals/viscous forces but no fractal geometry decreased the time of removal of the first peak from 30 to 45 min to about 20 min. Fig. 2c shows that further accounting for fractal geometry decreased the time to about 10 min. Although much uncertainty exists in the Hamaker constant, the fractal dimension versus particle size, and other parameters, the analysis here

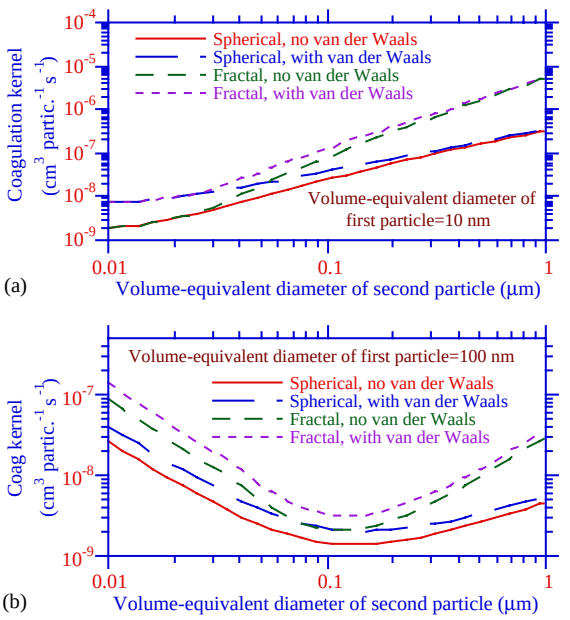

Fig. 4. Brownian coagulation when the volume-equivalent diameter of the first particle is (a) 10 nm and (b) 100 nm and the volume-equivalent diameter of the second particle varies from 10 to 1000 nm. The four curves shown in each figure account for when particles are spherical ($D_\mathrm{f} = 3$) or fractal ($D_\mathrm{f} = 1.7$) and when van der Waals and viscous forces are or are not included. The collision radius was set to the fractal radius. Also, $A/k_\mathrm{B}T = 200$, $T = 300\,\mathrm{K}$, and $p = 1\,\mathrm{atm}$.

suggests that the inclusion of van der Waals/viscous forces and fractal geometry may account for a greater share of the evolution of nanoparticle size than Brownian motion alone.

4. Three-dimensional evolution of the aerosol distribution

Three-dimensional point- and line-source simulations were next run for 4 min. The coagulation kernel in the simulations accounted for van der Waals forces and fractal geometry. Fig. 5 shows the near-surface horizontal wind field, solved prognostically, after 4 min in the point-source case. The wind field in the line-source case was similar.

Fig. 6a shows the horizontal distribution of the column abundance of the emitted soot and the sulfate-emitted soot distributions, time-averaged over the 4-min point-source simulation. Whereas, the emitted soot distribution peaked at the point of emission and tailed off with distance from the point, the peak of the sulfate-emitted soot distribution appeared downwind. This was expected since the only source of sulfate-emitted soot particles is heterocoagulation. The column abundance of sulfate-emitted soot is 2–3 orders of magnitude lower

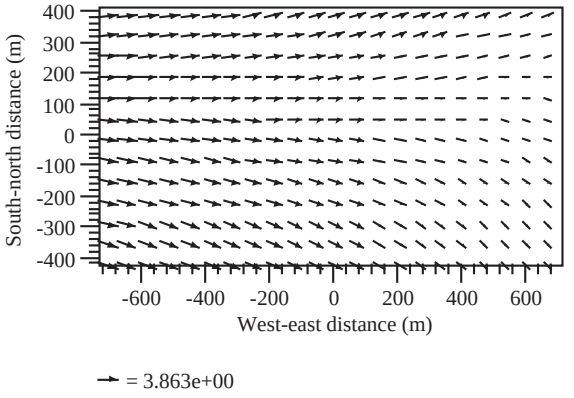

Fig. 5. Modeled near-surface wind field ($m\,s^{-1}$) after 4 min of simulation in the point-source simulation.

than that of emitted soot, suggesting that heterocoagulation of emitted soot with background sulfate is not rapid.

Fig. 7a shows the near-surface number concentration of particles of different size, summed over all distributions, versus west–east distance from the point of emission at the end of the point-source simulation. The figure shows that the number concentration of <25 nm particles decreased by a factor of 4 between 30 and 100 m downwind of emission. Zhu et al. (2002a, Fig. 7) showed a factor of 5 decrease between 30 and 100 m for both wind speed cases. Zhu et al., though, showed a slight increase in 25–50 nm particles between 30 and 100 m downwind in one case and only a small decrease in the second. Here, an increase was not seen, but the rate of decrease of 25–50 nm particles was less than that of 0–25 nm particles. As discussed previously, even with treatment of van der Waals/viscous forces and fractal geometry, the simulated coagulation rate was not so fast as that inferred from the Zhu et al. data.

Fig. 7b shows the difference between the result from Fig. 7a and the result when coagulation is ignored. The difference represents the number concentration of particles lost due to coagulation (as opposed to dilution) with distance. In the no-coagulation case, the number concentration of all particles from 0 to 30 m downwind decreased from 155,000 to 83,000 particles cm^{-3} after 4 min. At 30 m downwind, the difference in number concentration between the no-coagulation and the coagulation case was 1300 cm^{-3}, suggesting that about 2% of the decrease in particle concentration between 0 and 30 m at 4 min was due to coagulation and most of the rest was due to dilution (some was due to dry deposition as well). This result, though, depends substantially on the emission rate. For example, in a simulation in which emission rates was twice as high, coagulation reduced about 7%, and dilution, about 93%, of the number concentration 30 m to the east of emission.

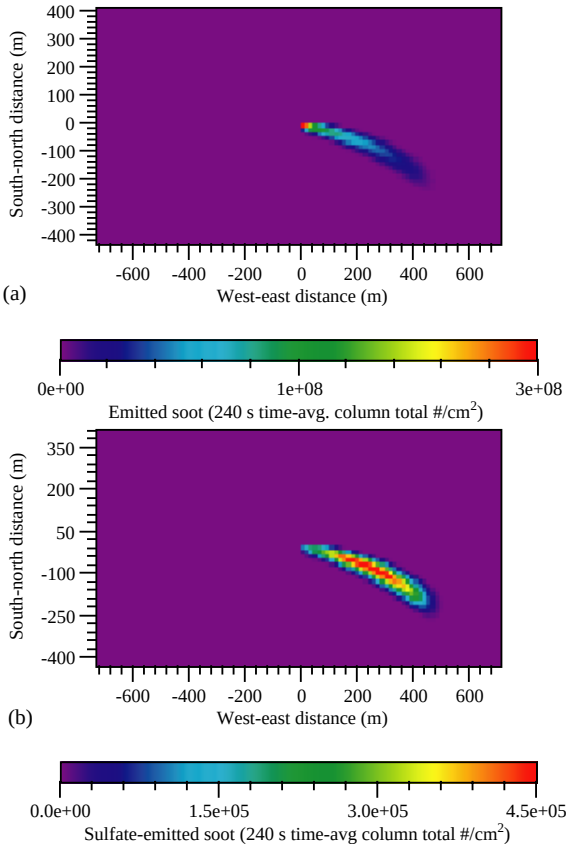

Fig. 6. Modeled column abundance of (a) the emitted soot distribution and (b) the sulfate-emitted soot distribution, time-averaged over the 4-min point-source simulation.

Fig. 7c shows the near-surface number concentration versus west–east distance for the sum of all heterocoagulated emitted-soot distributions (listed in figure caption) in the point-source case. Heterocoagulation produced new mixtures in increasing concentration with distance from the emission source. Heterocoagulation also produced more 25–50, 50–100, 100–220, and >220 nm particles than <25 nm particles. The maximum total number concentration of heterocoagulated particles produced at 4 min was 165 cm^{-3} and occurred near where the maximum number concentration was lost by coagulation (1300 cm^{-3}) suggesting that about 13% of coagulation loss near the emission sources was due to heterocoagulation and the rest was due to self-coagulation. Because the number of emitted particles decreases with distance downwind but the number of background particles generally does not, the relative fraction of total coagulation loss due to heterocoagulation can only increase (in the absence of new sources) as particles age. This hypothesis is supported with box simulations that found that, over a 4-h period, the number concentration

of emitted soot continuously decreased whereas that of the sum of heterocoagulated distributions continuously increased with time.

Fig. 7d shows the sum of all size distributions at the point of emission, 60 m to the east of emission, and 150 m to the east of emission at the end of the point-source simulation. The first peak in the summed distribution diminished with distance from the point of emission in favor of the second peak due to coagulation. This 3-D result is analogous to the box-model result in Fig. 2c, except that the 3-D result accounts for dilution, which lowers concentrations and slows coagulation in comparison with the 0-D case. A comparison of Fig. 8 with Figs. 4a and d of Zhu et al. (2002a) shows that, like in Zhu et al., the first peak diminishes in favor of the second peak 150 m downwind, but in that case, the decrease in the first peak is more pronounced than that found in the 3-D case here, possibly due in part to coagulation rates being slower here.

Fig. 7e shows the variation in the size distribution of sulfate-emitted soot (produced only by heterocoagulation) at three locations. Concentrations 60 m downwind exceed those at the point of emission for all sizes. The peak concentration of sulfate-emitted soot at 60 m is around 100 nm in diameter, which is slightly larger than the main peak in the initial sulfate distribution (Fig. 1) and than the largest peak in the emitted soot distribution. Although the submicron distribution of emitted soot is trimodal and that of background sulfate is somewhat bimodal, the distribution of sulfate-emitted soot is relatively unimodal as are the distributions of sea spray-emitted soot, soil-emitted soot, and background soot-emitted soot (not shown) because the size distribution formed by heterocoagulation most often takes the shape of the distribution of the larger particle in a coagulated pair. As such, small modes are not so prominent in heterocoagulated distributions.

Fig. 8 shows the horizontal distribution of near-surface emitted soot (Fig. 8a) and sulfate-emitted soot (Fig. 8b) number concentrations at the end of the 4-min line-source simulation. Figs. 9a and b show an altitude–longitude cross-section of emitted soot (Fig. 9a) and sulfate-emitted soot (Fig. 9b) number concentration at the same time. As with the point-source simulation, peaks in the sulfate-emitted soot distribution in the line-

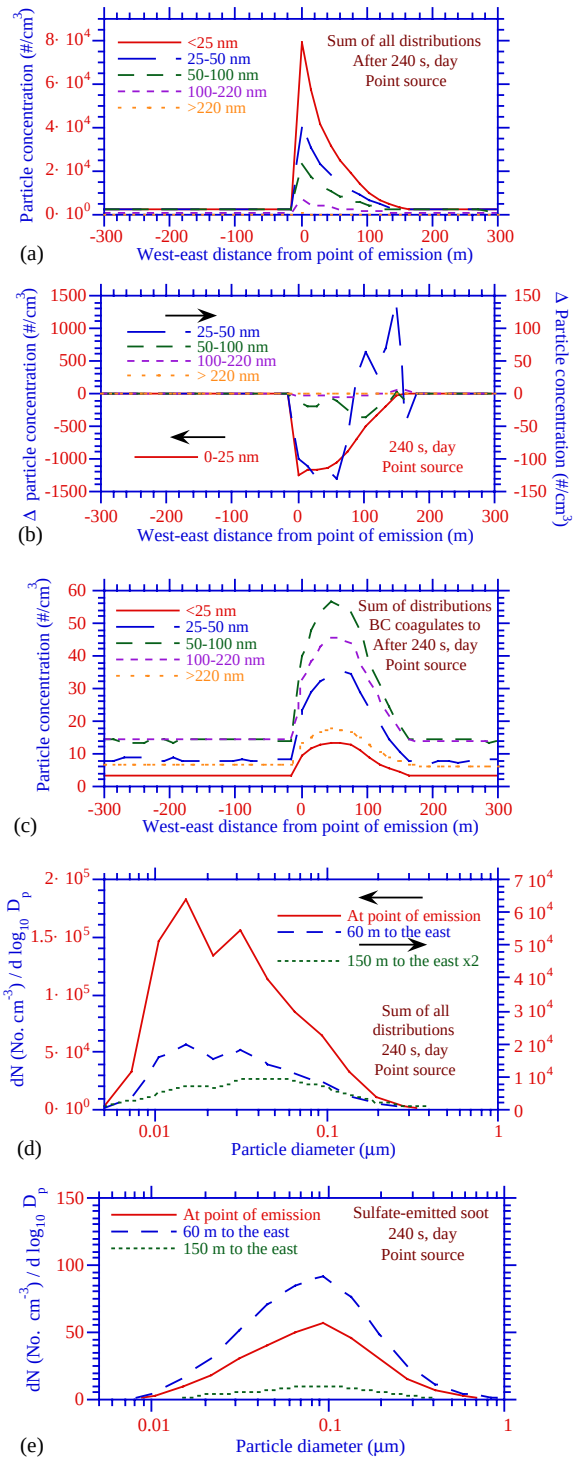

Fig. 7. (a) Near-surface number concentration of particles of different size, summed over all distributions, versus west–east distance at the latitude of the point of emission, at the end of the 4-min point-source simulation. (b) Difference between the result from (a) and that obtained when no coagulation was treated. This curve represents the net loss of particles of different size versus distance due to coagulation. (c) Same as (a), except for the sum of all distributions that emitted soot heterocoagulates to (sea spray-emitted soot, soil-emitted soot, sulfate-emitted soot, background soot-emitted soot, and internal mixture). (d) Sum of all size distributions at the point of emission, 60 m to the east of the emission, and 150 m to the east of emission at the end of the 4-min point-source simulation. (e) Same as (d), but for the sulfate-emitted soot distribution.

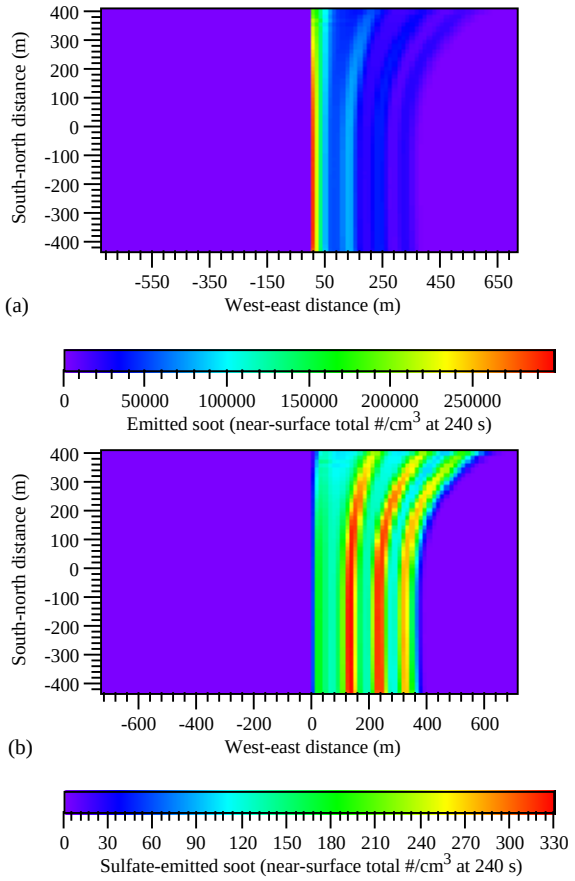

Fig. 8. Modeled near-surface number concentration of (a) the emitted soot distribution and (b) the sulfate-emitted soot distribution, at the end of the 4-min line-source simulation.

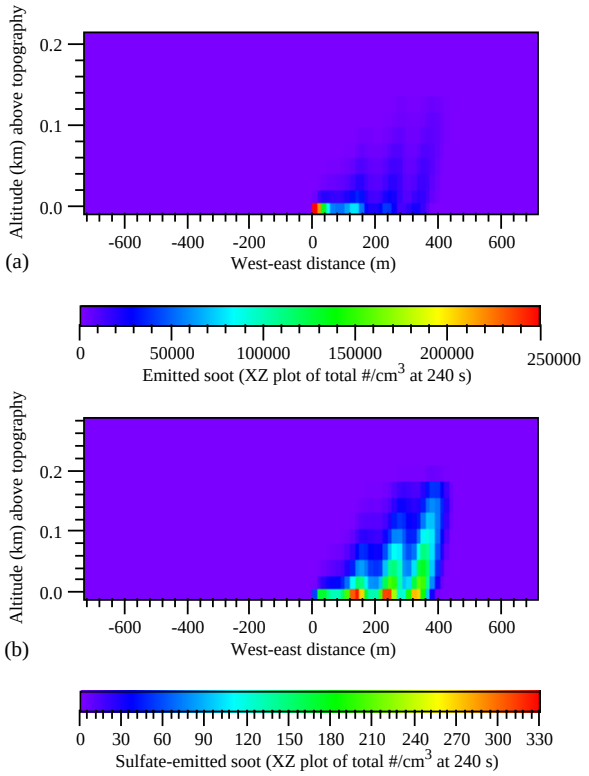

Fig. 9. Altitude–longitude cross-section (at the middle latitude of the grid) of the modeled number concentration of (a) emitted soot and (b) sulfate-emitted soot at the end of the 4-min line-source simulation.

source case occurred downwind of the main peak in the emitted soot distribution. Although the soot emission rate at each latitude was identical in this simulation, wind speed and direction varied with latitude (Fig. 5), causing a north–south concentration gradient at the northern end of the freeway by the end of the simulation (Fig. 8).

The wavelike variation in concentration downwind of emission in the line-source plots appears to be due to variations in vertical velocity downwind, resulting from the particular dynamical field generated by the simulation. For example, vertical velocities downwind of emission change direction from downward to upward, and location of the change moves during the simulation. Since peaks in emitted soot and sulfate-emitted soot occur at the same locations downwind (rather than peaks of emitted soot occurring together with troughs of sulfate-emitted soot), the concentrations of different distributions are transported together, also suggesting a dynamical rather than an aerosol microphysical cause of the waves. The waves occur in the absence of turbulence and dry deposition, so these processes are not the cause. Since the boundary layer is unstable and topography is uniform in this simulation, it is also unlikely that the waves formed are gravity waves. The line-source figures indicate that the waves formed are uniform and smooth. The waves do not appear to be numerical artifacts, since such artifacts would be expected to create instability and/or waves of high frequency, neither of which occurred here. The wavelike feature also appears in near-surface plots at the end of the point-source simulation (not shown), but not in the time-averaged column abundance plots shown in Fig. 6. The wavelike feature also occurs when the lowest model layer is set to 20 m rather than 5 m. In Fig. 9, most of the vertical dispersion was due to turbulence, since a sensitivity simulation in which turbulence was neglected resulted in hardly any transport of pollutants from the bottom layer to the second layer (but still resulted in the wavelike feature).

5. Conclusion

In this study, 0- and 3-D models were used to examine the evolution of multiple particle size distributions near

the source of emission. Some results were compared with those from field measurements near a freeway. It was found first that Brownian coagulation may be insufficiently fast to account for the rapid evolution of the summed aerosol size distribution observed in the field data. The enhancement of Brownian coagulation due to van der Waals/viscous forces and treatment of fractal geometry may account for a greater portion of the evolution. Uncertainty exists in parameters associated with these processes.

In the 3-D simulations, dilution was found to be more important than coagulation at reducing the total number concentration of particles near the source of emission, but the relative importance of dilution versus coagulation depends on concentration near the emission source. Results also show that heterocoagulation of emitted soot with background particles produced new mixtures in increasing concentration with distance from the emission source. Self-coagulation of emitted soot caused over an order of magnitude more particle loss than did heterocoagulation in the first few minutes after emission. Heterocoagulation, though, naturally increases in relative importance as particles age since the number of emitted particles decrease over time but the number of background particles generally does not.

Acknowledgements

This study was supported in part by the EPA Office of Air Quality Planning and Standards, the NSF Atmospheric Chemistry Division, and the NASA ACMAP program.

References

Abu-Allaban, M., Coulomb, W., Gertler, A.W., Gillies, J., Pierson, W.R., Rogers, C.F., Sagebiel, J.C., Tarnay, L., 2002. Exhaust particle size distribution measurements at the Tuscarora Mountain Tunnel. Aerosol Science and Technology 36, 771–789.

Ackerman, T.P., Toon, O.B., 1981. Absorption of visible radiation in atmosphere containing mixtures of absorbing and nonabsorbing particles. Applied Optics 20, 3661–3667.

Alam, M.K., 1987. The effect of van der Waals and viscous forces on aerosol coagulation. Aerosol Science and Technology 6, 41–52.

Artelt, C., Schmid, H.-J., Peukert, W., 2003. On the relevance of accounting for the evolution of the fractal dimension in aerosol process simulations. Journal of Aerosol Science 34, 511–534.

Association of European Automobile Manufacturers (ACEA), 1999. Programme on emissions of fine particles from passenger cars. ACEA Report, Brussels, December.

Capaldo, K., Pandis, S., 2001. Lifetimes of ultrafine diesel aerosol. Final Report for the University of Minnesota and the Coordinating Research Council under the E-43 Project Diesel Particulate Sampling Methodology.

Chung, S.H., Seinfeld, J.H., 2002. Global distribution and climate forcing of carbonaceous aerosols. Journal of Geophysical Research 107 (D19), 4407 (doi:10.1029/2001JD001397).

Chylek, P., Srivastava, V., Pinnick, R.G., Wang, R.T., 1988. Scattering of electromagnetic waves by composite spherical particles: experiment and effective medium approximations. Applied Optics 27, 2396–2404.

Fuller, K.A., Malm, W.C., Kreidenweis, S.M., 1999. Effects of mixing on extinction by carbonaceous particles. Journal of Geophysical Research 104, 15941–15954.

Gidhagen, L., Johansson, C., Strom, J., Kristensson, A., Swietlicki, E., Pirjola, L., Hansson, H.-C., 2003. Model simulation of ultrafine particles inside a road tunnel. Atmospheric Environment 37, 2023–2036.

Harris, S.J., Maricq, M.M., 2001. Signature size distributions for diesel and gasoline engine exhaust particulate matter. Journal of Aerosol Science 32, 749–764.

Hitchins, J., Morawska, L., Woff, R., Gilbert, D., 2000. Concentrations of submicrometre particles from vehicle emissions near a major road. Atmospheric Environment 34, 51–59.

Jacobson, M.Z., 1997. Development and application of a new air pollution modeling system. Part II: aerosol-module structure and design. Atmospheric Environment 31, 131–144.

Jacobson, M.Z., 2000. A physically based treatment of elemental carbon optics: implications for global direct forcing of aerosols. Geophysical Research Letters 27, 217–220.

Jacobson, M.Z., 2001. GATOR-GCMM: a global through urban scale air pollution and weather forecast model. 1. Model design and treatment of subgrid soil, vegetation, roads, rooftops, water, sea ice, and snow. Journal of Geophysical Research 106, 5385–5402.

Jacobson, M.Z., 2002. Analysis of aerosol interactions with numerical techniques for solving coagulation, nucleation, condensation, dissolution, and reversible chemistry among multiple size distributions. Journal of Geophysical Research 107 (D19), 4366 (doi:10.1029/2001JD002044).

Kasten, F., 1968. Falling speed of aerosol particles. Journal of Applied Meteorology 7, 944–947.

Kim, D., Gautam, M., Gera, D., 2002. Parametric studies of the formation of diesel particulate matter via nucleation and coagulation modes. Journal of Aerosol Science 33, 1609–1621.

Kittelson, D.B., 1998. Engine and nanoparticles: a review. Journal of Aerosol Science 6, 443–451.

Lu, R., Turco, R.P., 1995. Air pollutant transport in a coastal environment. II. Three-dimensional simulations over Los Angeles basin. Atmospheric Environment 29, 1499–1518.

Maricq, M.M., Chase, R.E., Podsiadlik, D.H., Vogt, R., 1999. Vehicle exhaust particle size distributions: a comparison of tailpipe and dilution tunnel measurements. SAE Paper 1999-01-1461, SAE International, Warrendale, PA.

Marlow, W.H., 1981. Size effects in aerosol particle interactions: the van der Waals potential and collision rates. Surface Science 106, 529–537.

Mellor, G.L., Yamada, T., 1982. Development of a turbulence closure model for geophysical fluid problems. Reviews of Geophysics and Space Physics 20, 851–875.

Mountain, R.D., Mulholland, G.W., Baum, H., 1986. Simulation of aerosol agglomeration in the free molecular and continuum flow regimes. Journal of Colloid and Interface Science 114, 67–81.

Mulholland, G.W., Samson, R.J., Mountain, R.D., Ernst, M.H., 1988. Cluster size distribution for free molecular agglomeration. Energy and Fuels 2, 481–486.

Naumann, K.-H., 2003. COSIMA-A computer program simulating the dynamics of fractal aerosols. Journal of Aerosol Science 34, 1371–1397.

Norbeck, J.M., Durbin, T.D., Truex, T.J., 1998. Measurement of primary particulate matter emissions from light-duty motor vehicles. Final Report for CRC Project No. E-24-2.

Okuyama, K., Kousaka, Y., Hayashi, K., 1984. Change in size distribution of ultrafine aerosol particles undergoing Brownian coagulation. Journal of Colloid and Interface Science 101, 98–109.

Pohjola, M., Pirjola, L., Kukkonen, J., Kulmala, M., 2003. Modelling of the influence of aerosol processes for the dispersion of vehicular exhaust plumes in street environment. Atmospheric Environment 37, 339–351.

Rogak, S.N., Flagan, R.C., 1992. Coagulation of aerosol agglomerates in the transition regime. Journal of Colloid and Interface Science 151, 203–224.

Sakurai, H., Tobias, H.J., Park, K., Zarling, D., Docherty, K., Kittelson, D.B., McMurry, P.H., Ziemann, P.J., 2003. On-line measurements of diesel nanoparticle composition and volatility. Atmospheric Environment 37, 1199–1210.

Schauer, J.J., Kleeman, M.J., Cass, G.R., Simoneit, B.R., 1999. Measurement of emissions from air pollution sources. 2. C1 through C30 organic compounds from medium duty diesel trucks. Environmental Science and Technology 33, 1578–1587.

Schmidt-Ott, A., Burtscher, H., 1982. The effect of van der Waals forces on aerosol coagulation. Journal of Colloid and Interface Science 89, 353–357.

Schnaiter, M., Horvath, H., Mohler, O., Naumann, K.-H., Saathoff, H., Schock, O.W., 2003. UV-VIS-NIR spectral optical properties of soot and soot-containing aerosols. Journal of Aerosol Science 34, 1421–1444.

Seinfeld, J.H., Pandis, S.N., 1998. Atmospheric Chemistry and Physics. Wiley-Interscience, New York.

Shi, J.P., Evans, D.E., Khan, A.A., Harrison, R.M., 2001. Sources and concentration of nanoparticles (<10 nm diameter) in the urban atmosphere. Atmospheric Environment 35, 1193–1202.

Steiner, D., Burtchnew, H., Grass, H., 1992. Structure and disposition of particles from a spark ignition engine. Atmospheric Environment 26, 997–1003.

Vignati, E., Berkowicz, R., Palmgren, F., Lyck, E., Hummelshoj, P., 1999. Transformations of size distributions pf emitted particles in streets. Science of the Total Environment 235, 37–49.

Wehner, B., Philippin, S., Wiedensohler, A., Scheer, V., Vogt, R., 2001. Volatility of aerosol particles next to a highway. Journal of Aerosol Science 32, S117–S118.

Weingartner, E., Keller, C., Stahel, W.A., Burtscher, H., Baltensperger, U., 1997a. Aerosol emission in a road tunnel. Atmospheric Environment 31, 451–462.

Weingartner, E., Burtscher, H., Baltensperger, U., 1997b. Hygroscopic properties of carbon and diesel soot particles. Atmospheric Environment 31, 2311–2327.

Wentzel, M., Gorzawski, H., Naumann, K.-H., Saathoff, H., Weinbruch, S., 2003. Transmission electron microscopical and aerosol dynamical characterization of soot aerosols. Journal of Aerosol Science 34, 1347–1370.

Zhu, Y., Hinds, W.C., Kim, S., Sioutas, C., 2002a. Concentration and size distribution of ultrafine particles near a major highway. Journal of the Air and Waste Management Association 52, 1032–1042.

Zhu, Y., Hinds, W.C., Kim, S., Shen, S., Sioutas, C., 2002b. Study of ultrafine particles near a major highway with heavy-duty diesel traffic. Atmospheric Environment 36, 4323–4335.